Journal of Materials Chemistry C

COMMUNICATION

View Article Online
View Journal | View Issue

Cite this: J. Mater. Chem. C, 2014, 2, 811

Received 9th October 2013
Accepted 5th November 2013

DOI: 10.1039/c3tc31987c

www.rsc.org/MaterialsC

Design of magnetoelectric coupling in a self-assembled epitaxial nanocomposite *via* chemical interaction†

Wen I Liang,[a] Yuangming Liu,[b] Sheng Chieh Liao,[c] Wei Cheng Wang,[d] Heng Jui Liu,[a] Hong Ji Lin,[de] Chien Te Chen,[e] Chih Huang Lai,[c] Albina Borisevich,[f] Elke Arenholz,[g] Jiangyu Li[b] and Ying Hao Chu*[a]

A chemically induced magnetoelectric coupling effect in ferroelectric/antiferromagnetic self-assembled vertical nanocomposites is designed. A concrete connection between chemical diffusion and the induced magnetic moment is revealed. Importantly, this study shows the strong magnetoelectric coupling effect, which is key to extend the design of functionality in vertical nanocomposites.

Introduction

Complex oxides, with rich physical properties along with superior chemical and thermal stabilities, have paved a new route for a number of advanced devices that cannot be achieved with conventional semiconductors.[1] In particular, as the precise control of nanomaterials synthesis developed during the 1990s, complex oxide heterostructures triggered a plethora of studies with novel phenomena in condensed matter, because they provide the possibility to integrate dissimilar oxides with diverse functionalities, and a feasible path to modulate the properties in strongly correlated electron systems.[2,3] From the material architecture aspect, there are various approaches to achieve heterostructures. Conventional multilayer or superlattice structures can be used as templates to easily manipulate film-on-substrate structures with tunable dimensions and a wide choice of compositions; however, this technique also has some limitations, such as poor accessibility to measure interfaces and limited interface area.[4] On the other hand, self-assembled vertical heterostructures, or nanocomposites, have enlarged the range of complex oxide heterostructures because they add additional architectural dimensions, generating high interface-to-surface ratios and enriching the structural, physical and chemical interaction phenomena.[3,5] For structural interactions, the effect of strain engineering, or the lattice mismatch between two phases, is the most important factor for epitaxial growth. Piezoelectricity–magnetostriction induced magnetoelectric (ME) coupling is one good example resulting from structural interaction which illustrates this concept. Well-known examples have been studied recently, such as the strong ME coupling due to the solid elastic interaction between $BaTiO_3$ and $CoFe_2O_4$,[6] as in the case of $BiFeO_3$–$CoFe_2O_4$.[7] Another phenomenon is physical coupling interactions, which occurs between parameters that are free from lattice strain. Take superconductivity coupled with the flux pinning effect as an example. This effect has been used to enhance the critical current in high temperature superconductors[8] and iron based superconductors.[9]

To date, the properties of self-assembled nanocomposites have been addressed structurally and physically. Studies of chemical interactions, or atomic interdiffusion, which is inevitable in two-phase systems, is, however, still missing so far. In fact, local element mixing can engender possibilities for the build-up of new functionalities based on the interaction of host and doped atoms. In order to explore this concept, this study reports the design of magnetoelectric coupling in an originally ferroelectric/antiferromagnetic material system: $BiFeO_3$ (BFO) and $LiMn_2O_4$ (LMO), a phenomenon which is induced by chemical interactions. LMO, an antiferromagnetic spinel at room temperature, was selected with the view that it can undergo complete substitution of manganese once one introduces another appropriate element, such as iron.[10] Iron doped lithium manganese oxide exhibits ferromagnetism

[a]Department of Materials Science and Engineering, National Chiao Tung University, HsinChu, 30010, Taiwan. E-mail: yhc@nctu.edu.tw
[b]Department of Mechanical Engineering, University of Washington, Seattle, WA 98195, USA
[c]Department of Materials Science and Engineering, National Tsing Hua University, Hsinchu 30013, Taiwan
[d]Graduate Program for Science and Technology of Accelerator Light Source, National Chiao Tung University, Hsinchu 30010, Taiwan
[e]National Synchrotron Radiation Research Center, 101 Hsin Ann Road, Hsinchu 30076, Taiwan
[f]Oak Ridge National Lab, 1 Bethel Valley Road, Oak Ridge, Tennessee, 37831, USA
[g]Advanced Light Source, 1 Cyclotron Road, Berkeley, California, 94720, USA

† Electronic supplementary information (ESI) available: Details of the *in situ* growth of self-assembled nanocomposite observed *via* RHEED, and high-resolution transmission electron microscopy investigations. See DOI: 10.1039/c3tc31987c

because Fe would contribute a net magnetic moment to lithium manganese oxide, and when all the Mn atoms are supplanted by Fe, namely lithium manganese oxide becoming lithium ferrite, it is a well-known ferromagnetic spinel oxide.[11] BFO, a ferroelectric perovskite at room temperature, was selected because it can supply enough iron atoms to the system; at the same time, the manganese in LMO can substitute directly into the B-site, which could enhance the magnetic properties of BFO to some extent according to a previous study.[12] That is, based on the compatibility of their elements, the $(BFO)_x$:$(LMO)_{1-x}$ self-assembled nanocomposite has been chosen as a model system to illustrate the chemical interactions between two phases.

Experimental section

In our study, the $(BFO)_x$:$(LMO)_{1-x}$ self-assembled nanocomposite was fabricated *via* a pulsed laser deposition (PLD) system equipped with a reflective high energy electron diffraction (RHEED) gun, which can monitor the deposition *in situ* (Fig. S1A†). The substrate we have chosen is $SrTiO_3$ (001) (STO) single crystal, and the growth was carried out at a temperature of 650 °C under an oxygen pressure of 100 mTorr. A KrF ($\lambda = 248$ nm) excimer laser was used, with energy 250 mJ at 10 Hz repetition rate. We used a self-made Bi–Fe–Li–Mn–O ceramic target as the deposition source. When Bi–Fe–Li–Mn–O species are stoichiometrically deposited onto the substrate, the RHEED pattern with suitable incident angle could give us information about the diffraction of the island crystal. In our case, the diffraction pattern matches that of the spinel structure, indicating that the island-like structure might be spinel (Fig. S1B†). After growth, the films were cooled down to room temperature at an oxygen pressure of approximately 760 Torr. For electric-related experiments, we first deposited a thin $SrRuO_3$ layer as the bottom electrode under the same conditions, and then the $(BFO)_x$:$(LMO)_{1-x}$ nanocomposite. The morphology was studied with a field emission scanning electron microscope (JEOL, JSM-6700F), and structural information was provided by a spherical aberration corrected scanning transmission electron microscope (Cs-TEM, JEOL ARM200F) and synchrotron-based X-ray diffraction (XRD) techniques. Reciprocal space maps (RSMs) were recorded using a PANalytical X'Pert Pro 4-circle X-ray diffractometer with Cu $K\alpha_1$ radiation ($\lambda = 1.54$ Å), and were recorded with a series of θ–2θ scans with different ω offsets. Surface chemical analysis was carried out using an Auger electron nanoscope (ULVAC-PHI, PHI 700) with nanoscale resolution. In order to understand the local magnetic element environment, polarization dependent soft X-ray absorption studies were performed at beamlines 4.0.2 and 6.3.1 at the Advanced Light Source (ALS) in the Lawrence Berkeley National Lab. In addition, the ferroelectric properties of the samples were examined by piezoforce response microscopy (PFM) using a scanning probe microscope (Vecco, Multimode 8). To characterize the ME coupling effect, we used an Asylum Research Variable Field Module (VFM), and details of the procedure can be found in our previous study.[13]

Results and discussion

From the series of scanning electron microscopy (SEM) images (Fig. 1(a)–(c)), as the content of BFO increases, the area of the island-like nanopillar decreases, indicating that the matrix is more likely formed from BFO and the nanopillar is formed from LMO. This finding was also discussed and proved by the calculation of surface energies in the perovskite–spinel system in a previous study.[14] The images were taken along the substrate edge, and the relative orientation of lattice match is indexed in the inset of Fig. 1(a). Another important characterization of the as-grown nanocomposite is X-ray diffraction (XRD) based reciprocal space mapping (RSM), which gives precise epitaxial relationship information. We consider the $(BFO)_{0.75}$:$(LMO)_{0.25}$ system by asymmetric RSM, for which relatively strained films (around 60 nm) were studied on the STO (103) plane. The planes following the STO substrate indicate the high quality of the nanocomposite, and only (103) BFO and (206) LMO peaks are observed. From Fig. 1(c), the lattice parameters of BFO are about 4.03 Å for the *c*-axis and 3.90 Å for the *a*-axis, implying that BFO is in-plane compressively strained by the STO substrate, with a cubic lattice constant of 3.905 Å; for the nanopillars, the lattice parameters of LMO are around 8.41 Å along the *c*-axis and 8.39 Å along the *a*-axis, indicating that the lattice constants of LMO are nearly isotropic, and much larger than the bulk value of 8.2 Å. According to the literature,[15–17] it is reasonable that the lattice constants of LMO increased when doped with iron atoms due to the substitution of Fe^{4+} (larger ionic radius) for Mn^{4+} (smaller ionic radius). Apart from the structural information, we employed another surface analysis technique, nano-Auger spectroscopy, to obtain chemical information. Fig. 1(e) shows one set of Auger mappings, with Bi (blue), Mn (green) and Fe (red) elements in the $(BFO)_{0.75}$:$(LMO)_{0.25}$ sample. If we correlate the surface and element mapping together, as in point 1

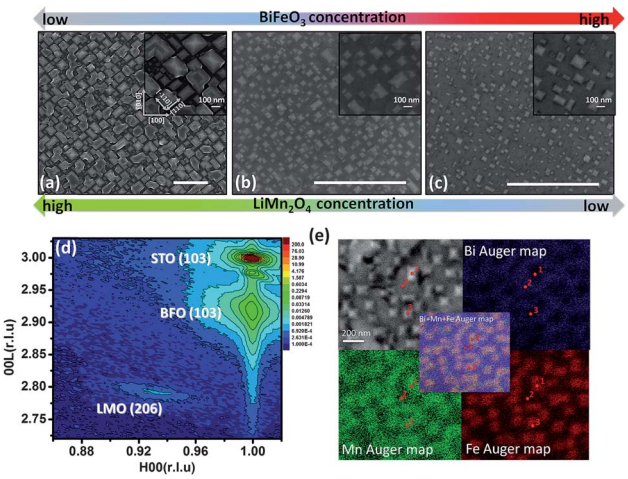

Fig. 1 (a)–(c) Top view SEM images of the nanocomposite with varying compositions (the scale bar equals 1 μm); (d) RSM mapping of the $(BFO)_{0.75}$:$(LMO)_{0.25}$ sample; (e) elemental sensitive Auger spectra mapping results.

(on the nanopillar), point 2 (on the matrix) and point 3 (on another nanopillar), we find that the nanopillars are located in Mn-rich regions, whereas the matrix is located in Bi-rich regions. However, the Fe element mapping result exhibits a rich region in nanopillars and a poor region in the matrix, which is the first direct evidence to prove that iron atoms indeed substitute into the nanopillars. That the relative concentration of Fe is higher in the nanopillars can be explained simply by the calculation of stoichiometry and mass conservation: let's assume that 30% Mn diffuses into BFO (which suggests that the approximate maximum amount for Mn-doped BFO retains ferroelectricity), the formula of the perovskite becomes $BiFe_{0.7}Mn_{0.3}O_3$ and the spinel becomes $LiMn_{1.1}Fe_{0.9}O_4$, and in this case, the distribution of Fe agrees with this assumption. Moreover, the Bi, Mn, and Fe Auger spectra are added up in the center of Fig. 1(e). Generally, iron and manganese are distributed more in the nanopillar than the matrix, in contrast to bismuth.

Microscopically speaking, the detailed structure of this epitaxial nanocomposite was studied *via* high resolution TEM (HR-TEM) (ESI, Fig. S2†). From the TEM study, we have also examined the composite distribution. The results show that the $(BFO)_{0.75}$:$(LMO)_{0.25}$ sample is composed of a $BiFe_{0.67}Mn_{0.33}O_3$ matrix and $LiMn_1Fe_1O_4$ nanopillars. Macroscopic properties are firmly connected with the microscopic behavior. According to previous studies, Fe doped LMO is ferromagnetic at room temperature, while if excess Mn is doped into BFO, the BFO crystal changes from a rhombohedral to an orthorhombic structure and destroys the ferroelectricity. In order to investigate the ferroelectricity, the piezoforce response microscopy (PFM) technique was employed in three samples. In PFM, we can use an external DC bias to "write" the polarization in a certain region and use a small AC bias to "read" the polarization change when the topology and the phase contrast are recorded simultaneously. Among those three samples, $(BFO)_{0.75}$:$(LMO)_{0.25}$ (sample A) and $(BFO)_{0.33}$:$(LMO)_{0.67}$ (sample C) show a polarization response, while sample B shows no polarization switching behavior. To clarify, the results of the $(BFO)_{0.75}$:$(LMO)_{0.25}$ sample are shown in Fig. 2(a) and (b). In Fig. 2(a), the figure on the right is the phase contrast signal; after we wrote the polarization up and down (by positive and negative DC bias), a brown-white phase contrast is shown, indicating the switching of polarization as well as the ferroelectricity. To specify, a sequence of DC voltages is applied on a single point in either the matrix or the nanopillars, and the piezoresponse is recorded simultaneously. In the matrix region, Fig. 2(b) shows the average butterfly loop of amplitude (A, blue line) and the hysteresis loop of phase (φ, red line) with applied bias, while the nanopillars show no such behavior. Without ambiguity, switching behavior is confirmed since the average phase contrast is close to 180°.

Another physical property studied here is ferromagnetism at room temperature. The total effect of the magnetic moment was collected by vibrating sample measurement (VSM), as shown in Fig. 2(c). As indicated, different colors represent different samples: the bold lines represent the hysteresis loop measured perpendicular to the film, and the normal lines were recorded lateral to the film. There is barely any ferromagnetic response in sample C, but a strong response is observed in samples A and B. Interestingly, the out-of-plane and in-plane hysteresis loops have nearly no anisotropic behavior, with squareness (ratio of residual moment to saturation moment) near to 0.5 in sample A; the saturation moment is around 80 emu cm^{-3} and the coercive field is around 250 Oe. On the other hand, sample B shows a strong anisotropy with the easy axis lying in-plane showing soft magnetic behavior, while the saturation moment is only a half of that in sample A.

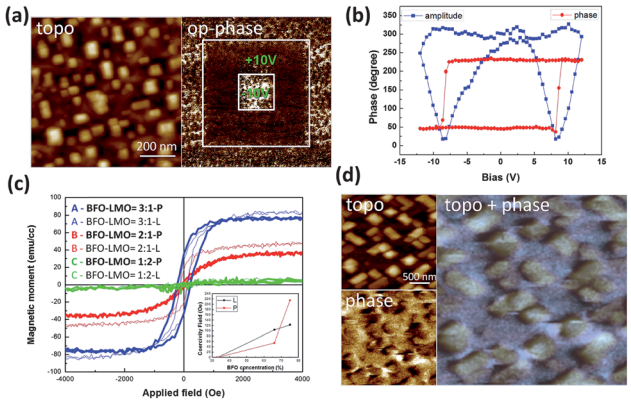

Fig. 2 Macroscopic characterization of ferroelectricity and ferromagnetism. (a) PFM of the $(BFO)_{0.75}$:$(LMO)_{0.25}$ sample; (b) the polarization switching behavior in the matrix region (blue: amplitude, red: phase signal); (c) M–H loop conducted by VSM technique; (d) the MFM image taken of the $(BFO)_{0.67}$:$(LMO)_{0.33}$ sample showing that the nanopillars have a strong magnetic response.

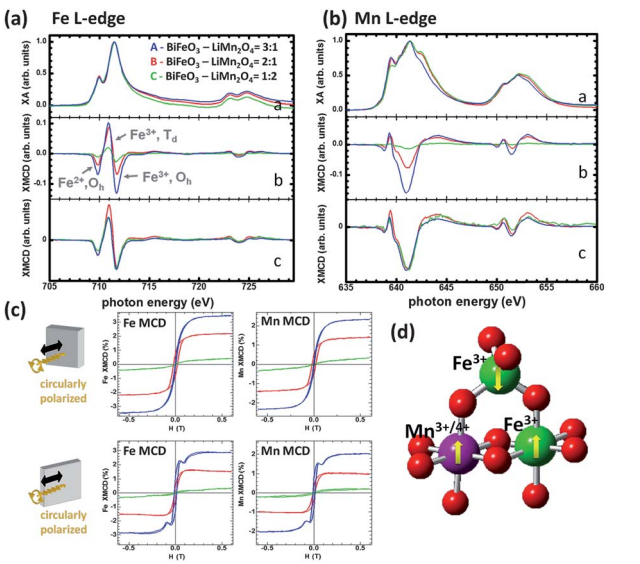

Fig. 3 (a) a: Fe $L_{3,2}$ XA spectra, b: XMCD spectra and c: XMCD spectra from b normalized to the same relative intensity as that of the Fe^{3+}, T_d XMCD feature. (b) a: Mn $L_{3,2}$ XA spectra, b: XMCD spectra and c: XMCD spectra from b normalized to the same relative intensity as that of the Mn $L_{3,2}$ XMCD feature. (c) The plot of XMCD signal as function of magnetic field; both in-plane and out-of-plane are shown. (d) The schematic of the Mn and Fe magnetic coupling relation.

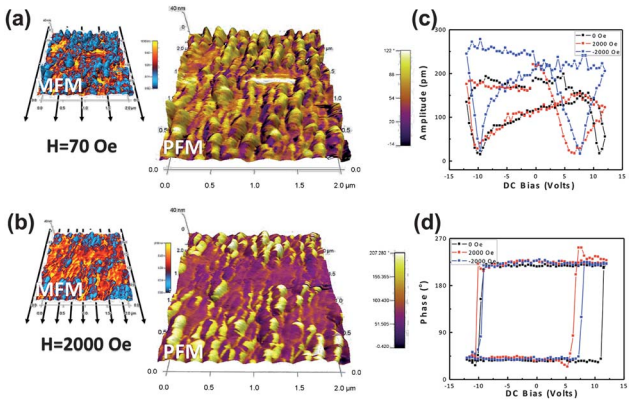

Fig. 4 The mapping of PFM and MFM as function of in-plane external magnetic field recorded by VFM; (a) images taken under 70 Oe; (b) images take under 2000 Oe. The switching characteristics of the piezoresponse in the matrix region affected by different in-plane external magnetic fields; (c) amplitude–bias butterfly loop; (d) phase–bias hysteresis loop.

Where does the region contribute to the magnetic moment? For nanoscale ferromagnetism, if we need to locate the magnetic region from the surface, magnetic force microscopy (MFM) fits our requirements. For MFM, the instrument was operated in a lift mode to detect the magnetic force acting between the cantilever tip and the surface of the samples, thus showing the phase difference. With the multi-domain structures, a pair of magnetic poles resulted in a brown-white contrast being observed in our samples (Fig. 2(d), in-plane phase). If we overlap the topology and the in-plane phase signal, we find that the nanopillars superimpose the phase contrast region, implying that the nanopillars show a stronger magnetic response than the matrix.

To determine the valence and spin states of Mn and Fe as a function of composition in the materials, we performed soft X-ray absorption spectroscopy (XAS) measurements at the Mn and Fe $L_{2,3}$ edges and obtained X-ray magnetic circular dichroism (XMCD) spectra, in which there is a difference between the X-ray absorption for circularly polarized light with the photon spin parallel (μ^+) and antiparallel (μ^-) to the external magnetic field applied parallel to the sample surface. XAS and XMCD signals at the transition metal $L_{2,3}$ edge is an extremely sensitive probe for the local environment of transition metal atoms. Fig. 3(a) and (b) show the results for the Mn-$L_{2,3}$ and Fe-$L_{2,3}$ spectra of each sample, respectively (blue for sample A, red for sample B, and green for sample C). From the XAS results, the valence states of Fe indicate a combination of Fe^{2+}, Fe^{3+} and Fe^{4+}, and for Mn, states of Mn^{2+}, Mn^{3+} and Mn^{4+}, indicating that the chemical reaction indeed occurs in this system. In order to compare the amounts contributed by Fe and Mn to the XMCD spectra, we can normalize the spectra of Fe and Mn to observe the intensity change. We found that the magnitude as well as the spectral shape of the Fe XMCD signal depends on the sample composition. With changing the BFO : LMO ratio, the change in the Fe XMCD spectral shape is indicative of differences in site occupancy of the Fe^{2+} and Fe^{3+} ions on sites with O_h and T_d symmetry. We have found, first, that when the composition of Fe increases, the MCD intensity also increases, as does the concentration of Fe T_d sites. According to the literature, the main contribution to the net magnetic moment in LMO comes from the Fe in tetragonal sites.[18,19] Moreover, the Fe XMCD signal decreases by approximately a factor of 2 between $(BFO)_{0.75}$:$(LMO)_{0.25}$ and $(BFO)_{0.67}$:$(LMO)_{0.33}$, and another factor of 3 from $(BFO)_{0.67}$:$(LMO)_{0.33}$ to $(BFO)_{0.33}$:$(LMO)_{0.67}$.

By contrast, the Mn XMCD spectral shape is nearly independent of sample composition and can be well described as combination of 20% Mn^{2+} and 80% $Mn^{3+/4+}$ mixed valence state, in which the Mn^{2+} is antiferromagnetically aligned to other Mn spins, as found in $La_{0.7}Sr_{0.3}MnO_3$.[20,21] The average Mn moment decreases with BFO content by a factor of 2 from $(BFO)_{0.75}$:$(LMO)_{0.25}$ to $(BFO)_{0.67}$:$(LMO)_{0.33}$, and by a factor of 5 from $(BFO)_{0.67}$:$(LMO)_{0.33}$ to $(BFO)_{0.33}$:$(LMO)_{0.67}$.

If we turn our attention to the crystal structure, in an ideal case, the possible positions for Fe are the following: octahedral sites in the perovskite, octahedral sites in the spinel, and tetrahedral sites in the spinel (responsible for net spins), while the possible positions for Mn are octahedral sites in the perovskite (also responsible for net spins), and octahedral sites in the spinel. Combined with our MCD spectra, we could obtain the both Mn and Fe MCD signals as a function of applied magnetic field parallel and perpendicular to the nanopillars (Fig. 3(c)), and the behavior implies the strong coupling effect between these two elements. Fig. 3(d) summarizes the schematic for the magnetic coupling relationship between Mn and Fe.

Since there are both ferroelectric and ferromagnetic species in our specific composition ($(BFO)_{0.75}$:$(LMO)_{0.25}$), the magnetoelectric coupling effect is established in this study. To visualize this effect, we have introduced a suitable approach with nanoscale resolution – variable field module (VFM). VFM allows us to apply an in-plane magnetic field to the nanocomposite, and detect the induced changes in the piezoforce response microscopy (PFM) at the same time.[13,22] The results of VFM are shown in Fig. 4, and both magnetic force microscopy (MFM) and PFM phase images are recorded. The applied in-plane magnetic fields are 70 Oe and 2000 Oe in Fig. 4(a) and (b), respectively. Along with the increase of external magnetic field, changes in PFM phase mapping as well as MFM phase mapping are clearly observed. In addition, the butterfly loop (Fig. 4(c)) and the hysteresis loop (Fig. 4(d)) are recorded in the matrix region with and without an external magnetic field. In the absence of a magnetic field, the coercive voltage is around 11 V. When the 2 kOe magnetic field is applied parallel and antiparallel, the coercive voltages shift to 6.5 V (parallel) and 8 V (antiparallel) respectively. The decrease in the coercive voltage indicates that the polarization switching is enhanced by a magnetic field, proving the magnetoelectric coupling effect.

Conclusions

We conclude this study by remarking on the chemical interactions between perovskite–spinel nanocomposites in a model system $(BFO)_x$:$(LMO)_{1-x}$, a ferroelectric/antiferromagnetic material. In this system, being a supplier, BFO induces the ferromagnetism in LMO. We have found that when the Fe

concentration is rich to some extent, the ferroelectric/ferromagnetic system can be generated at room temperature. Examination by XAS and XMCD techniques delineated the local environments of Mn and Fe, as well as their magnetic states. Furthermore, excitement in this study has been heightened by the strong magnetoelectric coupling effect visualized by the VFM technique. Therefore, we have delicately manipulated the chemical design between dissimilar oxide nanocomposites, resulting in a new functionality, which is key to extend the practical value of vertical nanocomposites.

Notes and references

1 S. A. Chambers, *Adv. Mater.*, 2010, **22**, 219–248.
2 H. Y. Hwang, Y. Iwasa, M. Kawasaki, B. Keimer, N. Nagaosa and Y. Tokura, *Nat. Mater.*, 2012, **11**, 103–113.
3 C. A. F. Vaz, J. Hoffman, C. H. Anh and R. Ramesh, *Adv. Mater.*, 2010, **22**, 2900–2918.
4 J. L. MacManus-Driscoll, *Adv. Funct. Mater.*, 2010, **20**, 2035–2045.
5 V. Moshnyaga, B. Damaschke, O. Shapoval, A. Belenchuk, J. Faupel, O. I. Lebedev, J. Verbeeck, G. Van Tendeloo, M. Mucksch, V. Tsurkan, R. Tidecks and K. Samwer, *Nat. Mater.*, 2003, **2**, 247–252.
6 H. Zheng, J. Wang, S. E. Lofland, Z. Ma, L. Mohaddes-Ardabili, T. Zhao, L. Salamanca-Riba, S. R. Shinde, S. B. Ogale, F. Bai, D. Viehland, Y. Jia, D. G. Schlom, M. Wuttig, A. Roytburd and R. Ramesh, *Science*, 2004, **303**, 661–663.
7 F. Zavaliche, H. Zheng, L. Mohaddes-Ardabili, S. Y. Yang, Q. Zhan, P. Shafer, E. Reilly, R. Chopdekar, Y. Jia, P. Wright, D. G. Schlom, Y. Suzuki and R. Ramesh, *Nano Lett.*, 2005, **5**, 1793–1796.
8 J. L. Macmanus-Driscoll, S. R. Foltyn, Q. X. Jia, H. Wang, A. Serquis, L. Civale, B. Maiorov, M. E. Hawley, M. P. Maley and D. E. Peterson, *Nat. Mater.*, 2004, **3**, 439–443.
9 S. Lee, C. Tarantini, P. Gao, J. Jiang, J. D. Weiss, F. Kametani, C. M. Folkman, Y. Zhang, X. Q. Pan, E. E. Hellstrom, D. C. Larbalestier and C. B. Eom, *Nat. Mater.*, 2013, **12**, 392–396.
10 P. P. Hankare, R. P. Patil, U. B. Sankpal, S. D. Jadhav, I. S. Mulla, K. M. Jadhav and B. K. Chougule, *J. Magn. Magn. Mater.*, 2009, **321**, 3270–3273.
11 E. Wolska, K. Stempin and O. Krasnowska-Hobbs, *Solid State Ionics*, 1997, **101**, 527–531.
12 J. K. Kim, S. S. Kim, E. J. Choi, W. J. Kim, A. S. Bhalla and T. K. Song, *J. Korean Phys. Soc.*, 2006, **49**, S566–S570.
13 S. H. Xie, Y. M. Liu, X. Y. Liu, Q. F. Zhou, K. K. Shung, Y. C. Zhou and J. Y. Li, *J. Appl. Phys.*, 2010, **108**, 054108.
14 H. Zheng, Q. Zhan, F. Zavaliche, M. Sherburne, F. Straub, M. P. Cruz, L. Q. Chen, U. Dahmen and R. Ramesh, *Nano Lett.*, 2006, **6**, 1401–1407.
15 P. P. Hankare, R. P. Patil, U. B. Sankpal, S. D. Jadhav, P. D. Lohande, K. M. Jadhav and R. Sasikala, *J. Solid State Chem.*, 2009, **182**, 3217–3221.
16 T. Tsuji, M. Nagao, Y. Yamamura and N. T. Tai, *Solid State Ionics*, 2002, **154**, 381–386.
17 T. Tsuji, H. Umakoshi and Y. Yamamura, *J. Phys. Chem. Solids*, 2005, **66**, 283–287.
18 Y. Li, B. Y. Ma, A. H. Wang, N. Chen, L. H. Liu, Y. Liu, W. P. Wang, X. X. Li, G. H. Cao, X. Q. Ma and J. Lu, *J. Phys.: Conf. Ser.*, 2011, **273**, 012117.
19 C. Wende, K. Olimov, H. Modrow, F. E. Wagner and H. Langbein, *Mater. Res. Bull.*, 2006, **41**, 1530–1542.
20 Y. Takamura, R. V. Chopdekar, E. Arenholz and Y. Suzuki, *Appl. Phys. Lett.*, 2008, **92**, 162504.
21 F. Yang, N. Kemik, M. D. Biegalski, H. M. Christen, E. Arenholz and Y. Takamura, *Appl. Phys. Lett.*, 2010, **97**, 092503.
22 S. H. Xie, F. Y. Ma, Y. M. Liu and J. Y. Li, *Nanoscale*, 2011, **3**, 3152–3158.